Principle of Stereoscopic Height Computations and their Applications to Stratospheric Cirrus over Severe Thunderstorms

By T. T. Fujita

Reprinted from the Journal of the Meteorological Society of Japan
Vol. 60, No. 1, February 28, 1982

Principle of Stereoscopic Height Computations and their Applications to Stratospheric Cirrus over Severe Thunderstorms

By T. Theodore Fujita

Department of Geophysical Sciences, University of Chicago
(Manuscript received 21 September 1981)

Abstract

An approximate but accurate method of stereo-height computations from overlapping images of geosynchronous satellites is presented. The method was applied to determine the height of ITCZ clouds from GMS-1 and GOES West images. The cloud-top topography of severe thunderstorms over the United States was obtained from GOES East and West images along with IR temperature measurements by both satellites. It was found that the IR temperature is 5 to 10°C warmer than the expected temperature of overshooting tops.

It is suspected that the warm IR temperature is caused by the stratospheric cirrus located 1 to 3 km above the anvil top, which was found repeatedly during the Lear Jet Experiment in 1971-1978. The cirrus is generated in the wake of overshooting tops as they sink violently into the anvil cloud. The radiometric characteristics of the cirrus uncouple the height-temperature relationship at the overshooting height, resulting in an uncertainty that the cloud-top warming may mean either sinking cloud top and/or increasing cirrus.

1. Introduction

Stereo-pair photographs prior to the space age were taken from low- and high-flying aircraft equipped with aerial mapping cameras. The aerial coverage for cloud mapping was limited because of the ceiling of the photographic altitude. TIROS 1, launched successfully on 1 April 1960, changed the photographic areas completely. Since then numerous overlapping pictures were obtained.

Ondrejka and Conover (1966) suggested the usefulness of the stereoscopic interpretation of NIMBUS II APT pictures. Basic problems in using APT pictures are their inevitable distortion, the lag in the picture time due to the orbital motion, and the large oblique angle of dual images. In spite of these problems Kikuchi and Kasai (1968) analysed NIMBUS II images over northern Japan, distinguishing sea ice from the clouds at several layers.

Apollo 6 pictures, free from distortion, were used extensively for stereo-height computations. Convective clouds over equatorial Africa on 4 April 1968 were contoured at 500 m intervals by Whitehead, *et al.* (1969) and an ITCZ cloud over southern Zaire was mapped by Shenk and Holub (1971). Several years later Shenk, *et al.* (1975) published a cloud-height contour map with 1 km contour intervals in color.

Apollo pictures are used in the stereoscopic mapping of the lunar surface. Over 18,000 overlapping pictures were taken by Apollo 8 and 10 through 17 during 1969-1972. For further detail refer to Masursky, *et al.* (1978). Likewise the surface of Mars, as reported by Carr and Evans (1980), and that of Mercury, by Dunne and Burgess (1978), have been mapped by using stereoscopic methods.

The use of geosynchronous satellites for stereo-height computations was first suggested by Bristor and Pichel (1974) of NESS (National Earth Satellite Service). They presented stereo-pair pictures by ATS 3 and SMS 1 located near 70°W and 45°W separated by 25° of longitude (rather small). They suggested the remapping of stereo-pair images onto Mercator projection in order to eliminate the earth's curvature for stereo viewing.

Since then NASA has emphasized the im-

portance of stereoscopic height measurements, leading to the development of the method by Minzner, *et al.* (1978). The major breakthrough in the stereo-mapping was reported by Hasler (1981), presenting a pair of remapped images and their combination in red and blue colors for stereo viewing with red and blue colored eyeglasses.

Presented in this paper are the concept of the stereo-height determination and the basic equations for computations. Several examples of analyses and their interpretations are also included along with the infrared temperature fields and the Lear Jet views of the tops of severe thunderstorms.

2. Stereoscopic parallax

The position of a cloud projected to the earth surface by the line of sight from a satellite moves around on the earth according to the viewing directions. C_E and C_W in Fig. 1 denote the apparent positions of a cloud projected to the sea level being viewed from the eastern and the western satellites. The true cloud is located at the intersection of the two lines of sight. To distinguish these apparent clouds from the true cloud, C_E is called the eastern cloud (apparent cloud seen by the eastern satellite) and C_W the western cloud.

The difference in the positions of these eastern and western clouds creates the stereoscopic parallax to be used for computing the height of the clouds seen in dual images obtained simultaneously.

Technically, the projection is performed by extending the lines of sight of a cloud to the surface of the terrestrial ellipsoid with its dimensions

Semimajor axis A=6378.388 km
Semiminor axis B=6356.912 km
Difference A−B=21.476 km

The geoid of the earth is locally higher or lower than the idealized ellipsoid. Recent measurements by satellite and terrestrial gravimetry indicate the existence of the high geoid near Palau Is. (+65 m), Canary Is. (+60 m), northern Chile (+45 m), etc., and the low geoid around Sri Lanka (−80 m), near Novosibirsk (−65 m), Hudson Bay (−55 m), etc. The inevitable error in stereo-height computations will be caused by the geoid shape which deviates from the ellipsoid.

The parallax vector in Fig. 1 is defined by its great-circle length P and its azimuth angle γ_P at the eastern cloud C_E. The azimuth angle is 90° when clouds are located either on the equator or on the mean subsatellite longitude of the eastern and the western satellites.

3. Terrestrial ellipsoid and spheroid

The terrestrial ellipsoid on x(equatorial) and y(pole to pole) coordinates is expressed by

$$\frac{x_e^2}{A^2}+\frac{y_e^2}{B^2}=1 \qquad (1)$$

where the suffix "e" refers to ellipsoid. The equation of the terrestrial spheroid in Fig. 2 is

$$x_s^2+y_s^2=A^2 \qquad (2)$$

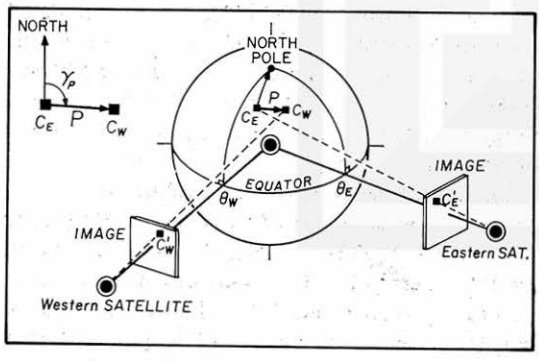

Fig. 1 Definition of the stereoscopic parallax, the vector connecting the western cloud C_W with the eastern cloud C_E which are the apparent clouds projected to the terrestrial sea level by western and eastern satellites.

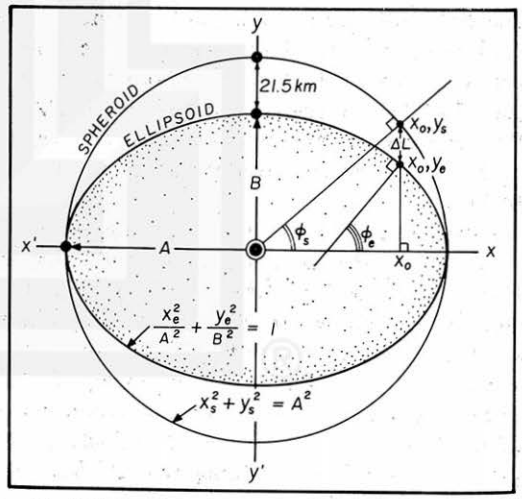

Fig. 2 Relationship between the spherical latitude ϕ_s and the ellipsoid latitude ϕ_e which is the true latitude on the map. ΔL is the stretch vector added to the ellipsoid to be stretched into spheroid.

where the suffix "s" refers to the terrestrial spheroid with its radius A.

The latitude on geographic maps denotes the angle of the local vertical measured from the equatorial plane. This latitude, also called the geodetic latitude, is identical to the ellipsoid latitude ϕ_e in Fig. 2.

The spheroid latitude ϕ_s at x_0, y_s is expressed by

$$\phi_s = \arctan\left(\frac{\sqrt{A^2-x_0^2}}{x_0}\right). \quad (3)$$

By differentiating the equation of ellipse in Eq. (1) with x_e, we obtain the ellipsoid latitude as

$$\phi_e = \arctan\left(\frac{A}{B}\frac{\sqrt{A^2-x_0^2}}{x_0}\right). \quad (4)$$

These equations show that the ellipsoid latitude is equal or larger than the corresponding spheroid latitude.

The difference $\Phi = \phi_e - \phi_s$, to be called the latitude correction, reaches the maximum value of 0.0966° or 10.74 km of arc at 45° latitude, north and south of the equator (See Table 1).

The increment of the latitude correction $d\Phi/d\phi$ can also be expressed by meters per degree of latitude. Computed values in Table 1 reveal the maximum value to be +374 m/deg at the equator, zero at 45° and −380 m/deg at the pole.

The vector quantity ΔL in Fig. 2, called the stretch vector, is parallel to the rotation axis of the earth. The length of the vector increases from zero at the equator to 21.5 km at the pole (see Table 1). The stretch vector is computed from

$$\Delta L = (A-B)\sin\phi_s. \quad (5)$$

It is feasible to compute the longitude and latitude of the point of intersection between the terrestrial ellipsoid and the sensor axis without approximation. To save computer time in projecting numerous clouds to the ellipsoid surface, the above mentioned spheroid-ellipsoid relationships can be used in performing approximate computations with a high degree of accuracy.

Fig. 3 presents three-dimensional geometry in which the terrestrial ellipsoid is stretched into the spheroid by adding the stretch vectors ΔL computed from Eq. (5).

Although satellite photographs are printed on flat paper, their coordinates are spherical coordinates centered at the satellite. Their axes are

- α *Scan angle*: the scan angle of the sensor provided by the spinning motion of satellite. Positive angle is measured from the image subpoint (ISP) toward the direction of the scan.
- β *Stepping angle*: the angle of the sensor axis provided by the stepping motor. Positive angle is measured northward from the scan equator.

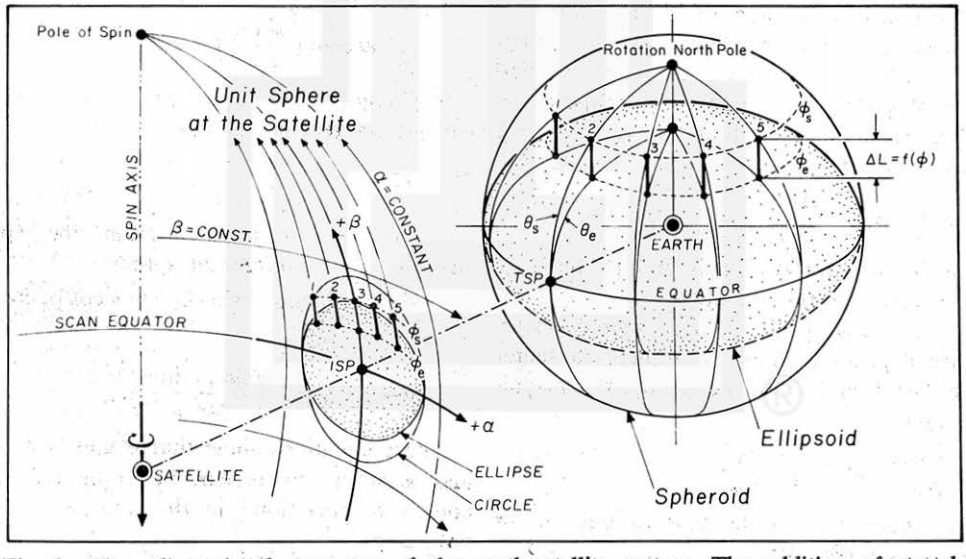

Fig. 3 Three-dimensional geometry of the earth-satellite system. The addition of stretch vectors turn the ellipsoidal earth into a spheroid meanwhile the elliptic image on the unit sphere stretches into a perfect circle.

The elliptic image of the terrestrial ellipsoid on $\alpha-\beta$ coordinates turns into a perfect circle when the ellipsoid is stretched by adding the stretch vector ΔL.

It should be noted that the stretch vector, parallel to the earth's rotation axis, coincides with the α-constant line on the $\alpha-\beta$ image coordinates. This means that the stretching does not alter the longitude. Consequently, no longitude correction is required when geographic grids are computed by using the terrestrial spheroid. Thus we write

$$\theta_e=\theta_s \tag{6}$$

where suffixes "e" and "s" refer to ellipsoid and spheroid, respectively.

Latitude correction is necessary because stretching does change the ellipsoid latitude ϕ_e into the spheroid latitude ϕ_s. After computing spheroid latitudes they can be converted into ellipsoid latitudes by combining Eqs. (3) and (4) into

$$\phi_e=\arctan\left(\frac{A}{B}\tan\phi_s\right). \tag{7}$$

Eqs. (6) and (7) permit us to compute ellipsoid latitudes and longitudes of clouds on image coordinates simply by intersecting the lines of sight with the terrestrial spheroid. No longitude correction is required, although latitude correction up to 0.1° should be made whenever necessary.

4. Computation of parallax

The first step of parallax computations is to convert the original photographic image on X-Y coordinates (on paper or film) into a circular image on $\alpha-\beta$ coordinates, keeping in mind that X is proportional to α and Y is proportional to β. The radius of the circular image on $\alpha-\beta$ coordinates is expressed by

$$\alpha_{\max}=\arcsin\left(\frac{A}{D}\right) \tag{8}$$

where A is the semimajor axis and D, the geocentric distance of the satellite.

Since $X_{\max}$ and $Y_{\max}$ on the original photograph are dependent upon the dimension factor applicable to X and Y independently, the magnification factors,

$$i=\frac{\alpha_{\max}}{X_{\max}} \quad \text{and} \quad j=\frac{\alpha_{\max}}{Y_{\max}} \tag{9}$$

should be computed in the unit of deg/cm or radian/cm (see Fig. 4).

The second step of parallax computations is to obtain longitudes and latitudes of eastern and western clouds projected to the terrestrial spheroid. For this purpose, we define the angles in Fig. 5.

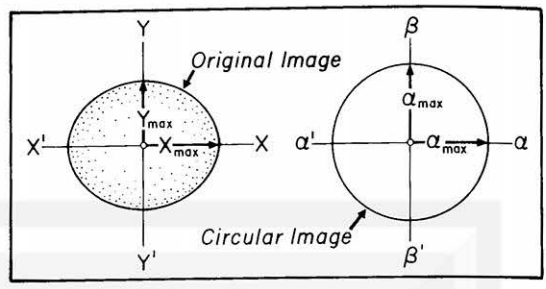

Fig. 4 Conversion of the original image into a circular image on α-β coordinates.

- ϕ sphere latitude of cloud, $\phi_.$ that of TSP (terrestrial subpoint)
- θ longitude of cloud, $\theta_.$ that of TSP
- $\gamma_.$ azimuth angle of cloud seen from TSP
- η nadir angle of cloud
- δ geocentric angle between TSP and cloud

The term "cloud" used in the description of these angles denotes either the eastern or western cloud projected to the spheroid surface.

Three-dimensional geometry of the earth-satellite system in Fig. 5 now permits us to compute θ and ϕ of eastern and western clouds by making use of the following equations:

Compute η and $\gamma_.$ from the right spherical triangle on the image sphere.

$$\eta=\arccos(\cos\alpha\cos\beta) \tag{10}$$

$$\gamma_.=\arctan\left(\frac{\sin\alpha}{\tan\beta}\right) \tag{11}$$

Compute $\delta=f(\eta, A, D)$ from the plane triangle on geocentric plane.

$$\delta=-\eta+\arcsin\left(\frac{D}{A}\sin\eta\right) \tag{12}$$

Compute θ and ϕ from the spherical triangle on the terrestrial sphere.

$$\phi=\arcsin(\cos\delta\sin\phi_.+\sin\delta\cos\phi_.\cos\gamma_.) \tag{13}$$

$$\theta-\theta_.=\arcsin\left(\frac{\sin\gamma_.\sin\delta}{\cos\phi}\right). \tag{14}$$

These equations show that θ and ϕ of eastern and western clouds can be computed from α and β of the cloud in the dual imagery, thus obtaining

ϕ_E and θ_E from α_E and β_E (15)

ϕ_W and θ_W from α_W and β_W (16)

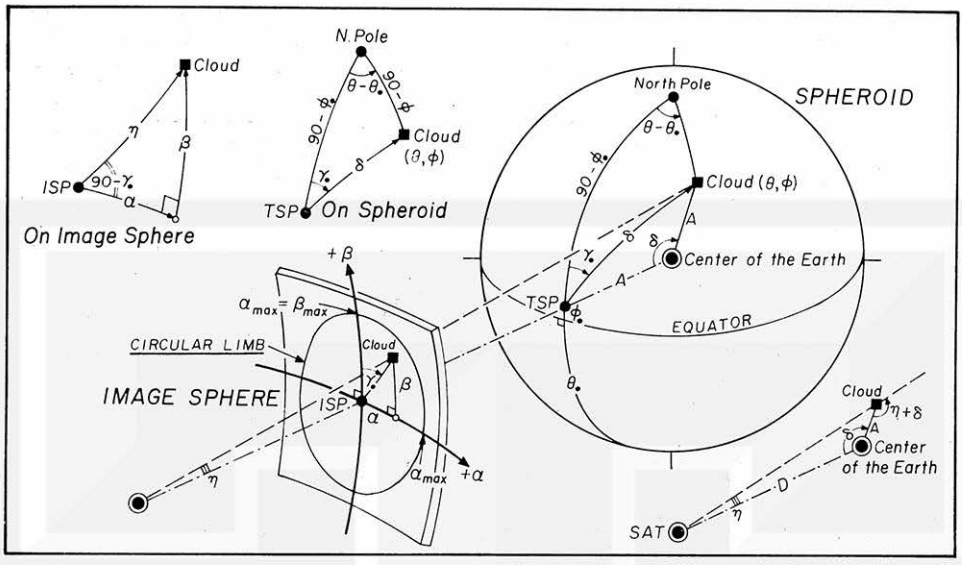

Fig. 5 Computation of θ and ϕ on the earth as functions of α and β on the image sphere centered at the satellite. Two spherical triangles and a plane triangle are solved to achieve computations.

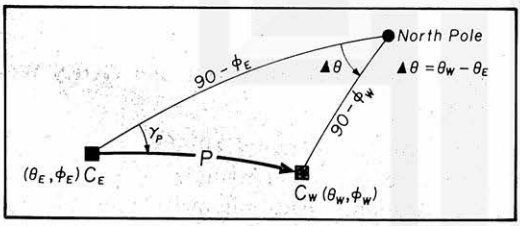

Fig. 6 Determination of stereo parallax vector as a function of computed longitudes and latitudes of eastern and western clouds.

where suffixes "E" and "W" refer to the eastern and the western cloud, respectively.

Within the areas of accurate parallax computations, the distance between C_E and C_W in Fig. 1 does not exceed one degree of arc on the earth. Furthermore, $\phi_W - \phi_E$ is only a small fraction of one degree so that the latitude correction is not necessary for parallax computations.

The parallax vector can be computed from the longitudes and the latitudes in Eqs. (15) and (16) by solving the spherical triangle in Fig. 6.

$$P = \arccos(\sin\phi_E \sin\phi_W + \cos\phi_E \cos\phi_W \cos\Delta\theta) \quad (17)$$

where $\Delta\theta = \theta_W - \theta_E$ denotes the longitudinal separation of the eastern and western clouds. The azimuth angle of the parallax is computed from

$$\gamma_P = \arcsin\left(\frac{\sin\Delta\theta \cos\phi_W}{\sin P}\right). \quad (18)$$

5. Unit parallax and height computation

The stereoscopic parallax at a given location is proportional to the cloud height, but the constant of proportionality varies with the separation of two satellites as well as the location of the cloud.

The unit parallax introduced in this paper is the parallax of the cloud located 10 km above the terrestrial ellipsoid which may be substituted by the spheroid for computation purposes because the latitude increment in Table 1 is

Table 1. Latitude correction $\Phi = \phi_e - \phi_s$ tabulated as a function of spheroid latitude ϕ_s. $d\Phi/d\phi$ is the increment of the latitude correction per degree of latitude and ΔL, the stretch vector.

ϕ_s deg	$\phi = \phi_e - \phi_s$ degree	km	$d\phi/d\phi$ m/deg	ΔL km
90	0.0000	0.00	−380	21.48
75	0.0482	5.38	−324	20.74
60	0.0836	9.32	−184	18.58
45	0.0966	10.74	0	15.16
30	0.0837	9.28	+188	10.71
15	0.0484	5.36	+326	5.54
3	0.0101	1.12	+372	1.12
2	0.0068	0.74	+373	0.75
1	0.0034	0.37	+374	0.37
0	0.0000	0.00	+374	0.00

extremely small. The unit parallax P_{10}, to be computed as a function of longitude and latitude, permits us to obtain the stereo height from

$$H=\frac{P}{P_{10}}\times 10\,\text{km} \tag{19}$$

where H denotes the height of the cloud with computed parallax P.

The unit parallax vector produced by the eastern and the western satellites with their subsatellite points at $\theta_{\cdot E}$, $\phi_{\cdot E}$ and $\theta_{\cdot W}$, $\phi_{\cdot W}$ is the vector sum of the individual parallax P_E and P_W in Fig. 7. Because the distance to the geosynchronous satellite is very large compared with cloud heights, the zenith angle of the satellite at the cloud top and at the subcloud point may be regarded as identical. The difference is usually less than 0.02°.

By using the zenith angle of the satellite at the eastern cloud C_E and that at the western cloud C_W, the individual parallax can be expressed by

$$P_E=10\tan\zeta_E \quad\text{and}\quad P_W=10\tan\zeta_W \quad\text{in km} \tag{20}$$

where suffixes "E" and "W" refer to the eastern and the western cloud, respectively.

The zenith angle is obtained by solving the geocentric, plane triangle in Fig. 7.

$$\zeta=\arcsin\left(\frac{D\sin\delta}{\sqrt{A^2+D^2-2AD\cos\delta}}\right) \tag{21}$$

where A is the semimajor axis, D the geocentric distance of satellite, and δ the geocentric angle from TSP to subcloud point.

The spherical triangle connecting the north pole, subcloud point, and TSP is used to obtain

$$\delta=\arccos(\sin\phi_{\cdot}\sin\phi+\cos\phi_{\cdot}\cos\phi\cos\Delta\theta) \tag{22}$$

where $\Delta\theta=\theta-\theta_{\cdot}$. The same spherical triangle is used in computing the azimuth angle of eastern cloud C_E and that of western cloud C_W as

$$\gamma_E=\arcsin\left(\frac{\cos\phi_{\cdot E}\sin\Delta\theta_E}{\sin\delta_E}\right) \tag{23}$$

$$\gamma_W=\arcsin\left(\frac{\cos\phi_{\cdot W}\sin\Delta\theta_W}{\sin\delta_W}\right) \tag{24}$$

where $\Delta\theta_E=\theta-\theta_{\cdot E}$ and $\Delta\theta_W-\theta_{\cdot W}$.

Finally, the length of the unit parallax vector is computed from

$$P=\sqrt{(M_W-M_E)^2+(N_W-N_E)^2} \tag{25}$$

where

$$M_W=P_W\sin\gamma_W \quad\text{and}\quad M_E=P_E\sin\gamma_E$$
$$N_W=P_W\cos\gamma_W \quad\text{and}\quad N_E=P_E\cos\gamma_E.$$

By using the above expressions, the azimuth angle of the unit parallax vector is given by

$$\gamma_P=\arctan\left(\frac{M_W-M_E}{N_W-N_E}\right). \tag{26}$$

Eqs. (20) through (26) permit us to compute unit parallax vectors at any location on the earth within the dual views of two geosynchronous satellites.

6. Stereo heights from GMS-1 and GOES West imagery

GMS 1 at 140°E and GOES West at 135°W are separated by 85° longitude. It is a rather large separation. The minimum unit parallax occurring on the equator at 177.5°W is 24.4 km, indicating that the top of a 10 km tall cloud there is projected as eastern and western clouds 24 km apart.

As shown in Fig. 8, the area of the overlapping images extends from the east of Guam to the

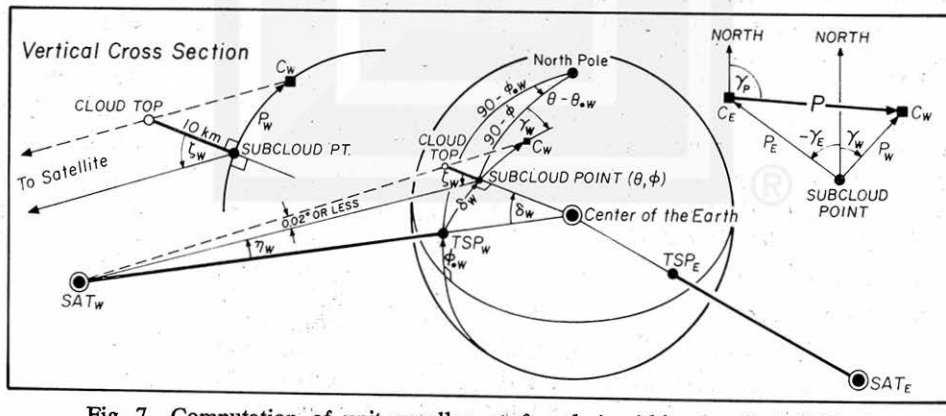

Fig. 7 Computation of unit parallax at θ and ϕ within the dual field of view of eastern and western satellites.

east of Hawaii and from the Bering Sea to the south of New Zealand. The azimuth angle of the unit parallax is mostly between 85° and 95° so that the unit parallax vector points eastward. If a computed vector deviates significantly from the expected direction we should suspect the wrong identity of cloud pairs in the two images.

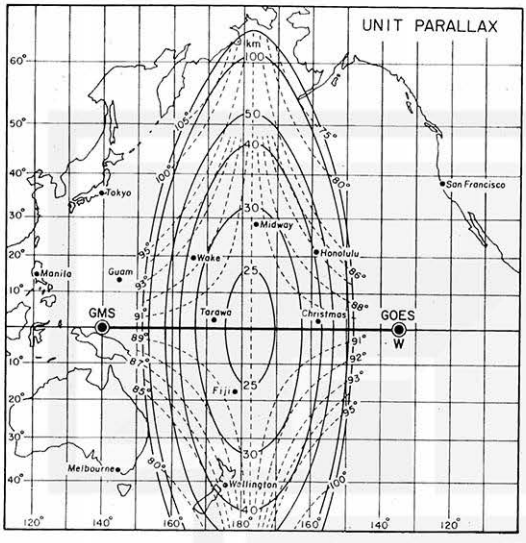

Fig. 8 Unit parallax produced by GMS 1 (140°E) and GOES West (135°W) separated by 85° of longitude. Vectors are expressed by their lengths in km and the azimuth angles in degrees.

Fig. 9 shows the distribution of ITCZ clouds at 0123 GMT 26 November 1980 photographed by GOES West. *A*, *B*, *C*, *D* denote the reference areas of low clouds where cloud heights are expected to be 1 to 4 km. Heights of the holes in overcast are measured in areas *I* and *J* while *K* through *N* represent the areas of outflow cirrus.

Results of height computations are shown in Fig. 10 in which stereo heights are plotted in kilometers superposed upon the cloud pattern in the stereo-pair GMS 1 picture. Measured heights in Table 2 reveal that the reference clouds in areas *A*, *B*, *C*, *D* are mostly of low clouds. Holes in the overcast are 1 to 2 km lower than the outflow cirrus.

7. Stratospheric cirrus documented by Lear Jet Experiments

Lear Jet Experiments in 1971-1978 were conducted in an attempt to document the behavior

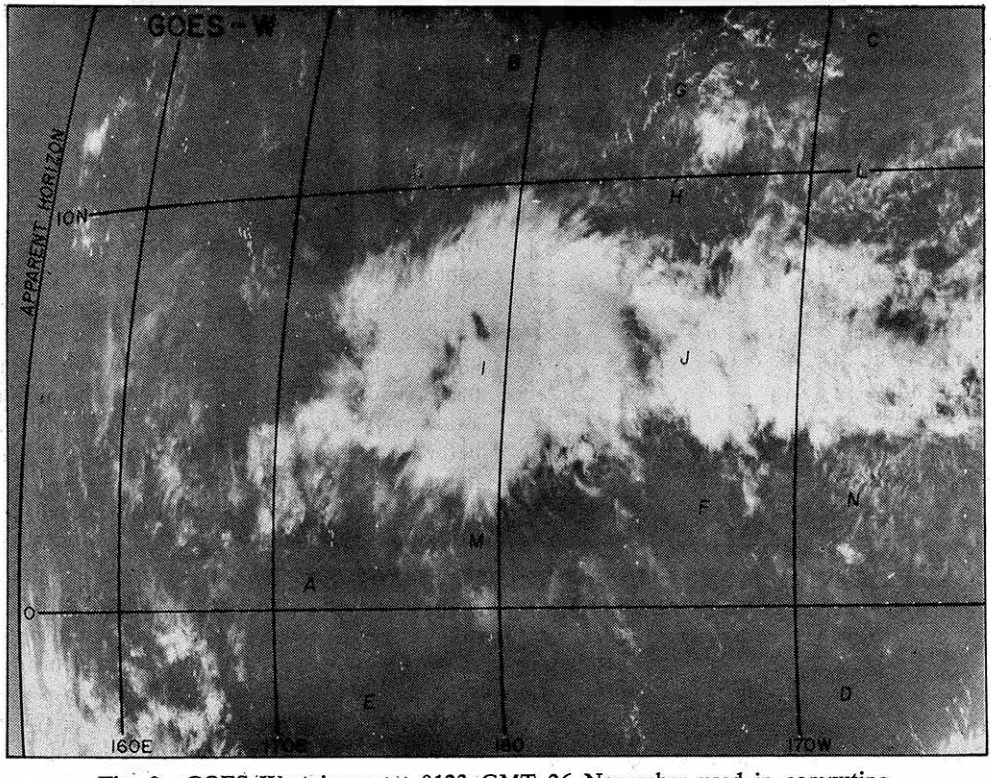

Fig. 9 GOES West image at 0123 GMT 26 November used in computing stereo heights with a simultaneous GMS 1 picture as the stereo pair.

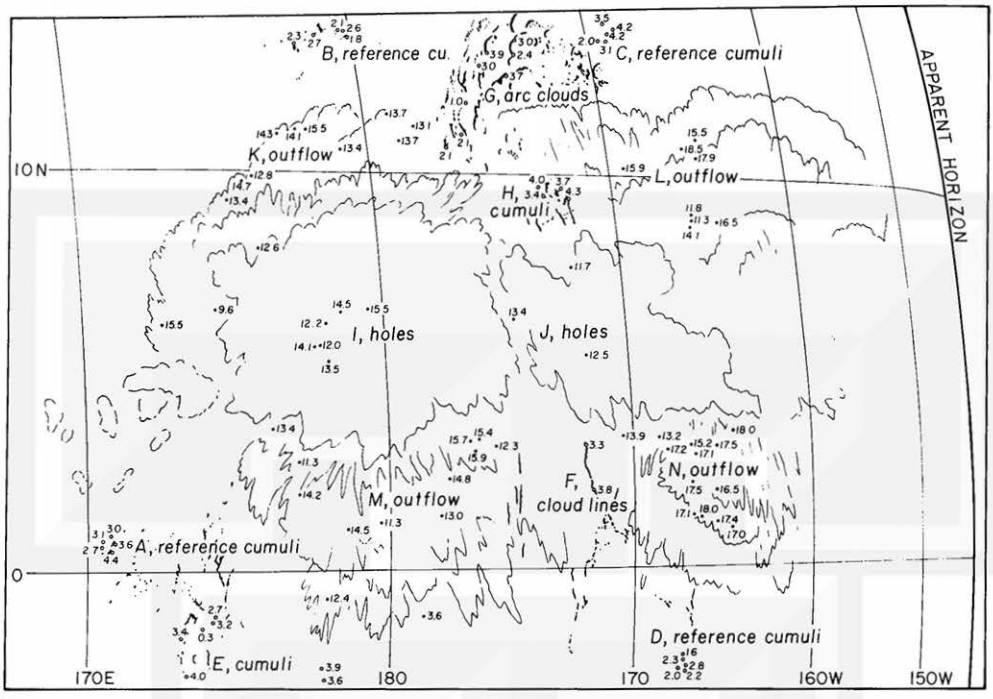

Fig. 10 Stereo heights plotted on the GMS 1 cloud analysis at 0123 GMT 26 November 1980.

Table 2. Statistics of cloud heights at 0123 GMT 26 November 1980 computed from stereo-pair photographs of GMS 1 and GOES West separated by 85° longitude.

	No. of Pairs	Stereo Heights (km) Min.	Mean	Max.
Low clouds				
A, Reference Cu	5	2.7	3.4	4.4
B, Reference Cu	5	1.8	2.3	2.7
C, Reference Cu	5	2.0	3.4	4.2
D, Reference Cu	5	1.6	2.2	2.8
E, Cumuli	7	0.3	3.0	3.9
F, Cloud Line	2	3.3	3.5	3.8
G, Arc Clouds	8	1.0	2.7	3.9
H, Cumuli	4	3.4	4.9	4.3
Mean of above		1.7	3.0	3.8
Holes in overcast				
I, Holes	6	12.0	13.6	15.5
J, Holes	2	12.5	13.0	13.4
Mean of above		12.3	13.4	15.0
Outflow cirrus				
K, Outflow Ci	11	12.6	13.8	15.5
L, Outflow Ci	8	11.3	15.2	18.5
M, Outflow Ci	12	11.3	13.7	15.9
N, Outflow Ci	13	13.2	16.6	18.0
Mean of above		12.2	14.9	16.5

of the overshooting domes above the anvil clouds of severe thunderstorms. One of the most striking features seen repeatedly above the anvil top is the formation of the cirrus cloud which jumps upward from behind the overshooting dome as it collapses violently into the anvil cloud. The cirrus cloud located above the anvil top inside the lowermost stratosphere is called the stratospheric cirrus.

The top photograph in Fig. 11 is a horizontal view of the stratospheric wake cirrus which extends downwind 27 km (inside the photo) or more. Some wake cirrus extends inside the stratosphere as far as 100 to 200 km downwind before becoming too thin to be seen from a high-flying Lear Jet.

From late spring to summer, westerlies above the anvil top decrease with altitude. The higher the cirrus, the slower its movement. Quite often, high cirrus moves upwind relative to the overshooting dome which creates the cirrus. It is in these seasons that a significant amount of the stratospheric cirrus is accumulated above the anvil top inside the wake region of the overshooting domes. The maximum height of the cirrus observed during the Experiments was 3.5 km above the anvil top.

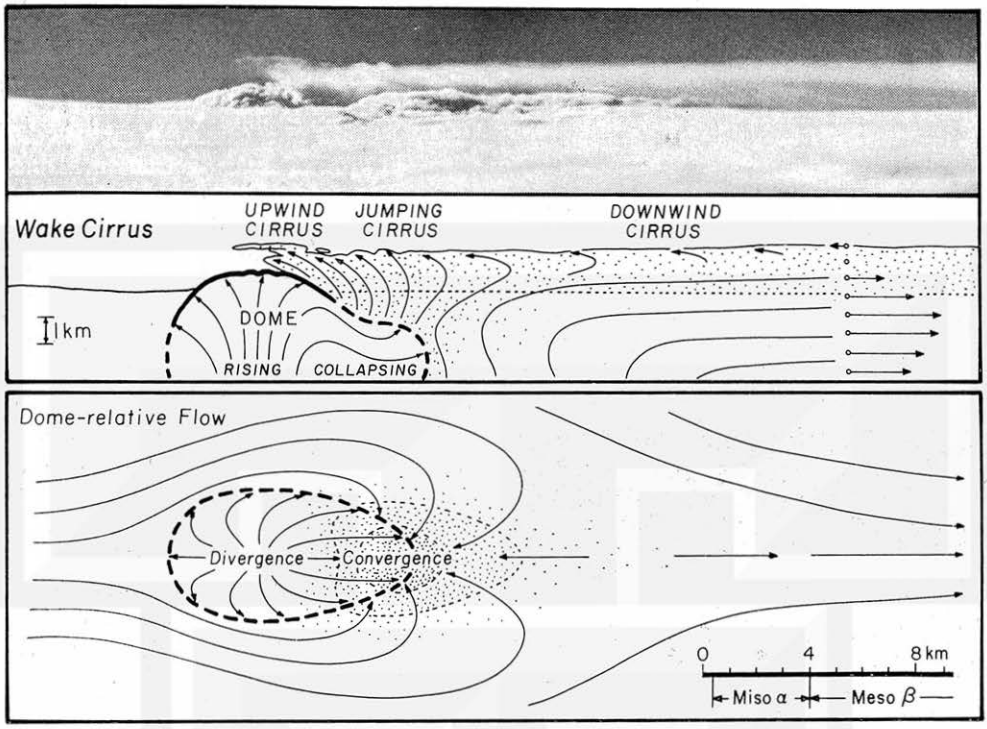

Fig. 11 A horizontal view of the stratospheric wake cirrus on 12 May 1972 from a research Lear Jet flying at 13.7 km over Texas with the author on board. Schematic diagrams show how cirrus clouds jump upward in the wake of a collapsing meso-Beta scale dome.

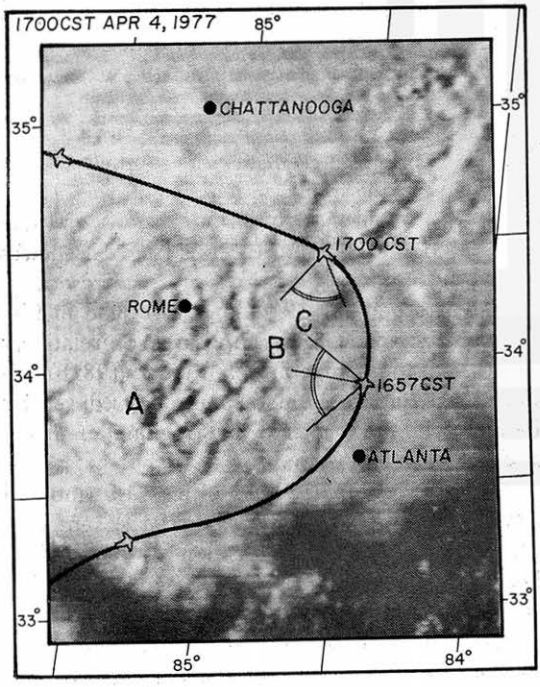

Fig. 12 GOES East image of the hook-echo thunderstorm of 4 April 1977. A research Lear Jet at 13.7 km MSL with the author on board flew around the hook-echo top indicated by the latter "A". The hook was monitored by the airborne radar during the approach phase.

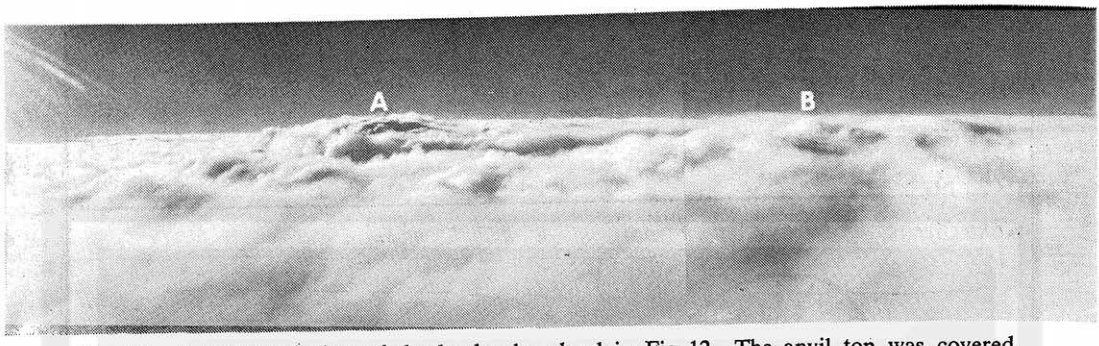

Fig. 13 A horizontal view of the hook-echo cloud in Fig. 12. The anvil top was covered, in part, with dense cirrus clouds located above the tropopause.

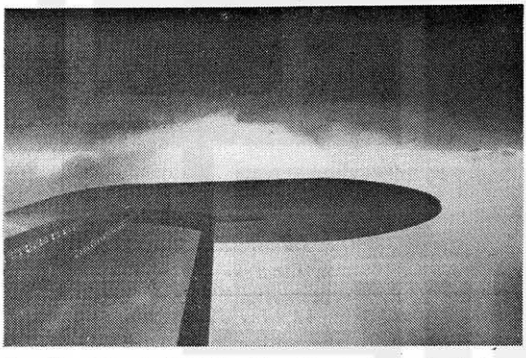

Fig. 14 Cloud "C" in Fig. 12 photographed from the Lear Jet as it flew near by. This picture indicates that some dome-like clouds atop the anvil may as well be the cirrus or cirrus-covered dome as seen in this picture.

During winter and early spring, on the other hand, westerlies increase with height above the anvil top. Consequently, the stratospheric cirrus is blown away before accumulating above the anvil top. Satellite pictures in Fig. 12 was taken on 4 April 1977 when westerlies above the anvil top were relatively strong. Cloud *A* in the picture was a hook-echo thunderstorm and *B* and *C* were small domes.

These tops were photographed from the research Lear Jet while flying around the activity area. Cloud *A* is characterized by a large overshooting dome with its edge covered with thin cirriform clouds. The overshooting top *B* in Fig. 13 is surrounded by cirrus and *C* in Fig. 14 is covered entirely with cirrus. These tops are 0.5 to 1 km higher than the Lear Jet flying at 13.7 km MSL. If the temperature of the cirrus is close to the environmental air temperature in the lowermost stratosphere, it should be considerably warmer than that of the overshooting, undiluted dome. Such warm cirrus over an extremely cold dome will increase the IR temperature of the dome significantly even if the emissivity of the cirrus is relatively small.

8. Anvil tops of severe thunderstorms

Stereoscopic heights of the 2 May 1979 storms over the Midwest were computed from the stereo-pair images of GOES West and East located at 135°W and 75°W, respectively. A large number of stereo-pair pictures, mostly at 3-minute intervals, were taken on that day which was one of the SESAME 1979 days.

Height computations were performed by using a picture pair at 2217 GMT, 2 hr 34 min earlier than the 0051 GMT picture time of the Bulletin-cover photograph by Hasler (1981). The computed stereo heights in km were plotted on the GOES East imagery in Fig. 15 in order to depict the cloud-top topography inside the expanding anvil.

Two mesocyclones, each with a tornado in progress, were located near the southwest edge of the anvil where the stereo height was 15 to 16 km MSL. The horizontal dimensions of these tall cloud domes fall into the Meso β scale newly defined by Fujita (1981a).

The corresponding IR temperature field in Fig. 16 is characterized by a large area of relatively warm anvil-top temperature. Fujita (1981b) assumed that the anvil-top warming was caused by the obstacle flow around the region of strong updrafts of mesocyclones.

A careful comparison of Figs. 15 and 16 reveals, however, that there is a large temperature gradient across the location of the highest cloud top depicted by the stereo heights, implying that the height-temperature relationships on the upwind and the downwind sides are significantly different. Fig. 17 was constructed in order to quantify these relationships.

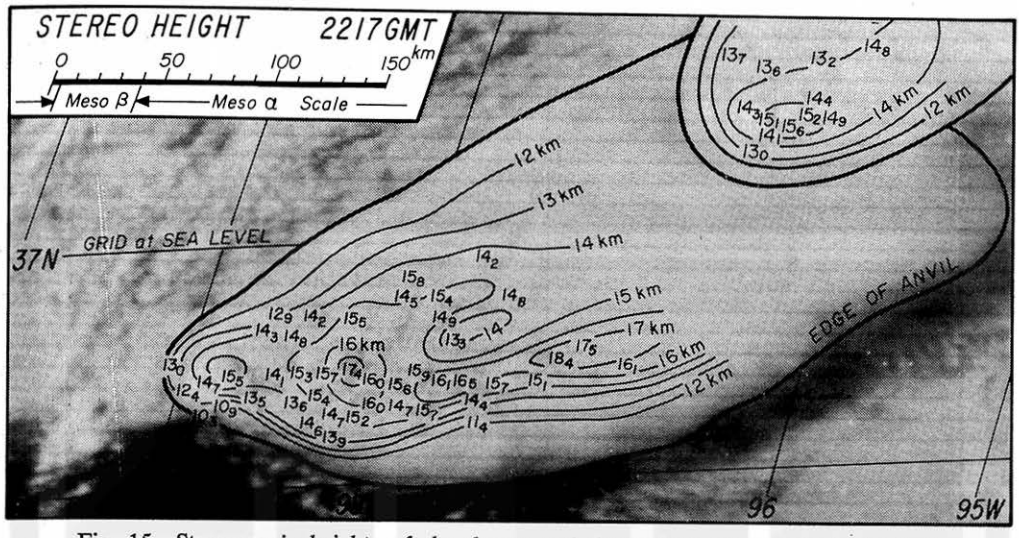

Fig. 15 Stereoscopic heights of the domes and depressions on the anvil cloud at 2217 GMT 2 May 1979. Measured heights were plotted in km (large numbers) and 0.1 km (small number) unit on the GOES visible imagery.

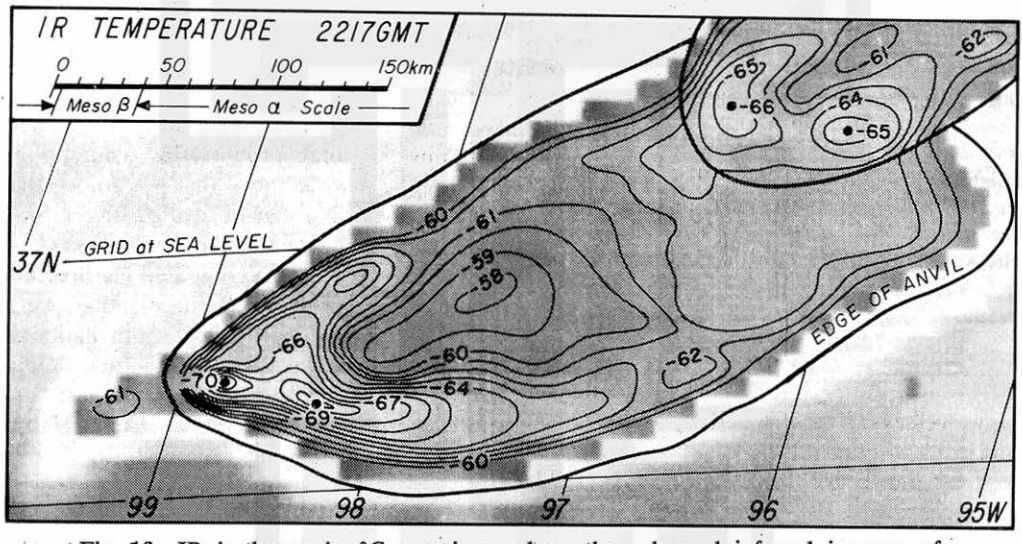

Fig. 16 IR isotherms in °C superimposed on the enhanced infrared imagery of GOES East at 2217 GMT 2 May 1979. The extensive warm area in the wake of over-shooting regions is called the *V* wake.

In plotting the height vs temperature diagram, the anvil area was divided into two regions separated by the horseshoe-shaped zone of large temperature gradient. Cloud tops and holes in the upwind region were plotted with open circles and those in the wake region with painted circles. It is seen that the clouds in the upwind region are 5 to 10°C colder than those in the wake region at the comparable stereo height.

The 8-km resolution (at TSP) of GOES IR sensor does not permit us to determine the temperature of individual tops and holes. Nevertheless, the horizontal dimensions of the warming area in Fig. 16 is 40 to 100 km, the smaller half of the Meso α scale. This scale of warming is large enough to be mapped by the sensor resolution.

The cause of the anvil-top warming in the wake region is most likely to be the stratospheric cirrus which is warmer than the overshooting dome at the comparable height. In warm seasons, when the westerlies above the anvil top are

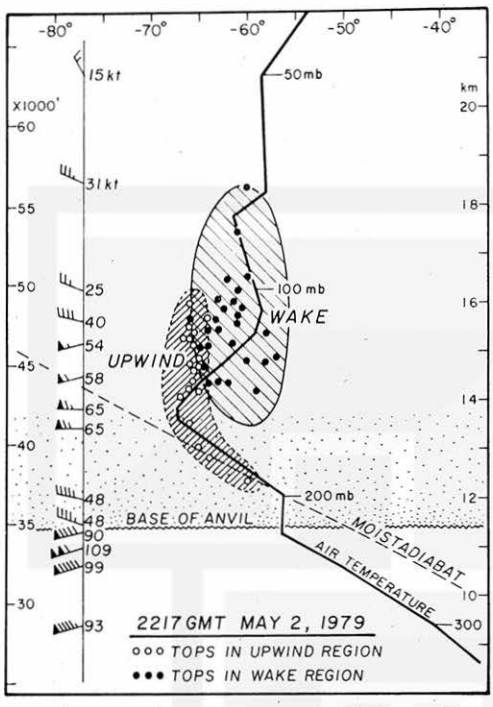

Fig. 17 IR-temperature vs. stereo-height diagram showing the anvil-top clouds in both upwind and downwind (wake) regions. Clouds with low heights are either depressed spots or holes at the anvil top. It is suspected that the tops in the wake region are covered with stratospheric cirrus clouds which are significantly warmer than the overshooting domes at the comparable height.

relatively weak, the high-level cirrus does remain in the wake region of the active domes which rise and collapse violently.

The Lear Jet Experiments during the 1970s confirmed repeatedly the existence and the extent, both vertical and horizontal, of the stratospheric cirrus. Since then, numerous *V*-shaped warm areas were seen in enhanced IR pictures of severe thunderstorms over the Midwestern United States. The *V*-shaped wake above the Grand Island tornado cloud of 3 June 1980 analysed by Fujita (1981b) was very significant, lasting for several hours.

9. Conclusions

Stereography of cloud-height computations from space-based photographs has made significant progress during the past 15 years. Cloud heights, both tops and holes, can now be computed with 1 km or better accuracy by using mini to regular computers available to most universities and research organizations. The cost of computations is only a few cents per cloud.

More sophisticated remapping programs of stereo-pair pictures developed by NASA now permit us to view three dimensional cloud features on color print, on projection screens, or on color TV by using colored eyeglasses. Fig. 18 is a detailed map of the cloud-top topography of the 3 May 1979 thunderstorm. Contour lines at 100 m intervals were drawn by the author based on Hasler's (1981) stereo-pair photographs.

The infrared temperature of anvil clouds larger than the instantaneous field of view (IFOV) has been used as a measure of the cloud height above the tropopause. However, the stereo height vs IR temperature relationships revealed during the past year now revoke their simplified correspondence in translating cold IR temperatures into overshooting heights.

Fujita and Wakimoto (1981) and many others have attempted to explain the anvil-top warming at or prior to the onset of downbursts and/or tornadoes under the assumption that these windstorms occur when overshooting domes collapse and sink into the anvil cloud. In the light of stereo-height computations, this assumption will have to be revised now that we know that an anvil-top warming can be caused either by sinking domes or increasing cirrus clouds.

Stereographic height computations presented in this paper lead to a conclusion that we must undertake an organized effort, both national and international, in investigating thermal, radiative, microphysical, and dynamical aspects of the stratospheric cirrus clouds by using high-flying aircraft and meteorological satellites.

Acknowledgements

The research presented in this paper has been sponsored by the National Aeronautics and Space Administration under Grant NGR 14-001-008 and the National Oceanic and Atmospheric Administration under Grant NOAA NA80AA-D-00001.

Research on stereo-height computations was performed in cooperation with Mr. Linwood Whitney of National Earth Satellite Service, NOAA and Dr. Fritz Hasler of Goddard Space Flight Center of NASA. Their cooperation in all aspects of the research is highly appreciated.

The stereo-pair pictures of GMS 1 and GOES West were taken under NASA-Japan Cooperative Program, achieving the required synchronization

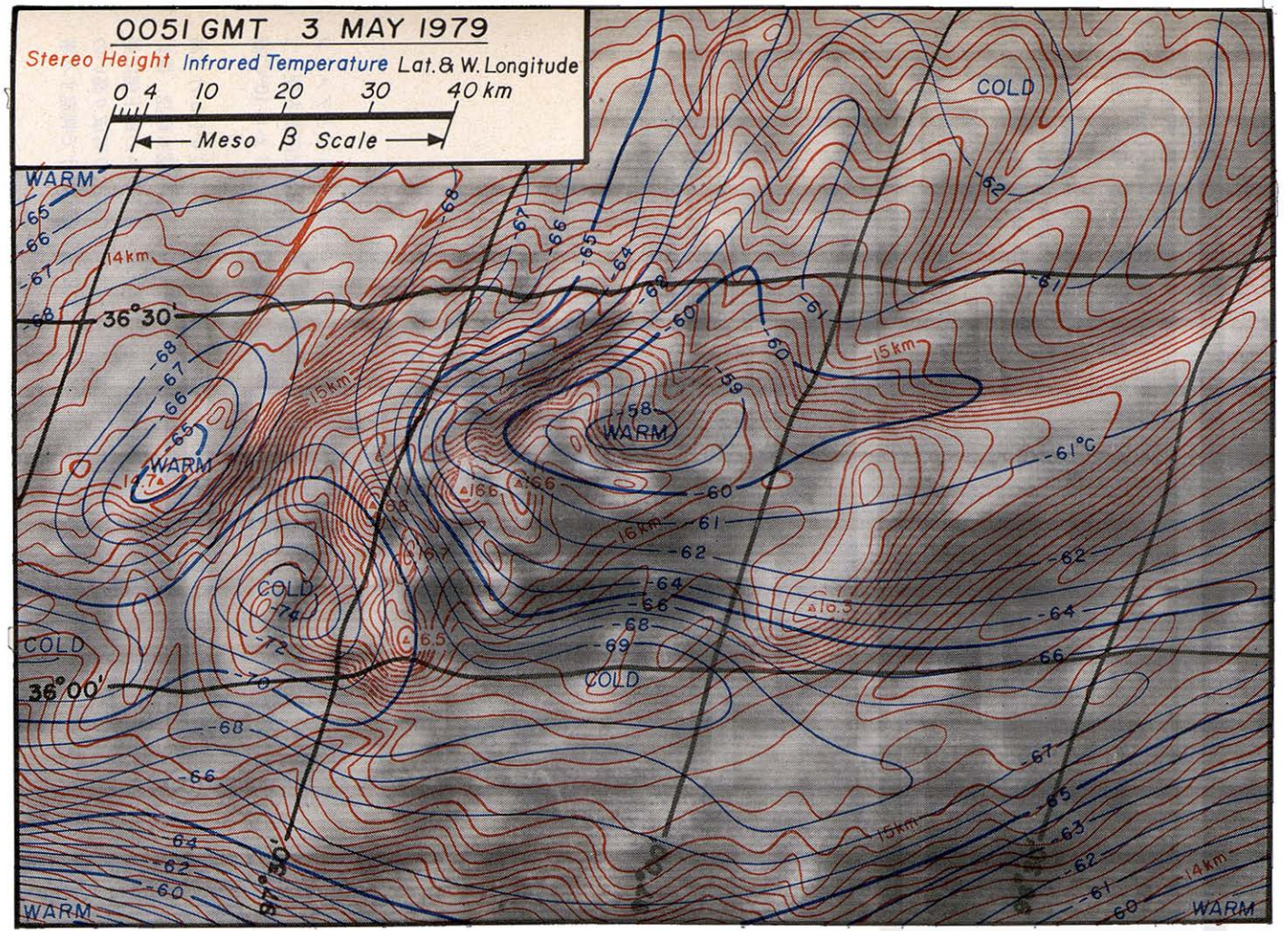

Fig. 18 A detailed topographic map of a thunderstorm top depicted by 100 m contour lines drawn by the author based on the stereo-pair pictures by Hasler (1981), computations of 67 stereo heights within the picture area, and the shadow effects on the anvil. IR temperature across the overshooting area increases as much as 17°C from the upwind to the downwind side.

through the direct telephone communication between the author and Mr. Kazuo Watanabe of the Meteorological Satellite Center at Kiyose. The cooperative program has been carried out under the leadership of Dr. Keikichi Naito of the Meteorological Research Institute at Tsukuba, Japan and Dr. James C. Dodge of NASA Headquarters at Washington, D.C.

References

Bristor, C. L. and W. Pichel, 1974: 3-D cloud viewing using overlapped pictures from two geostationary Satellites. *Bull. Amer. Meteor. Soc.*, **55**, 1353-1355.

Carr, M. H. and N. Evans, 1980: Images of Mars: The Viking extended mission. NASA SP-444, 32 pp. U.S. Gov. Pr. Office, Wash. D.C. 20402.

Dunne, J. A. and Burgess, 1978: The Voyage of Mariner 10: Mission to Venus and Mercury. NASA SP-424, 224 pp. U.S. Gov. Pr. Office, Wash. D.C. 20402.

Fujita, T. T., 1981a: Tornadoes and downbursts in the context of generalized planetary scales. *J. Atmos. Sci.*, **38**,

————, 1981b: Mesoscale aspects of convective storms. Proc. IAMAP Symposium. Hamburg, Germany. Nowcasting, 3-10.

———— and R. M. Wakimoto, 1981: Five scales of airflow associated with a series of downbursts on 16 July 1980. *Mon. Wea. Rev.*, **109**, 72-90.

Hasler, A. F., 1981: Stereographic observations from geosynchronous satellites: An important new tool for the atmospheric sciences. *Bull. Amer. Meteor. Soc.*, **62**, cover and 194-212.

Kikuchi, K. and T. Kasai, 1968: Stereoscopic analysis of photographs taken by NIMBUS II APT system. *J. Meteor. Soc. Japan*, **46**, 60-67.

Masursky, H., G. W. Colton, and F. El-Baz, 1978: Apollo over the Moon: A view from the orbit. NASA SP-362, 255 pp. U.S. Gov. Pr. Office, Wash. D.C. 20402.

Minzner, R. A., W. E. Shenk, J. Steranka, and R. D. Teagle, 1976: Stereographic cloud heights from imagery of SMS/GOES satellites. *Geophy. Res. Letters*, **5**, 21-24.

Ondrejka, R. J. and J. H. Conover, 1966: Note on the stereo interpretation of NIMBUS II APT photography. *Mon. Wea. Rev.*, **94**, 611-614.

Shenk, W. E. and R. J. Holub, 1971: An example of detailed cloud contouring from Apollo 6 photography. *Bull. Amer. Meteor. Soc.*, **52**, cover and p. 238.

Shenk, W. E., R. J. Holub, and R. A. Neff, 1975: Stereographic cloud analysis from Apollo 6 photographs over a cold front. *Bull. Amer. Meteor. Soc.*, **56**, 4-16.

Whitehead, V. S., I. D. Browne, and J. G. Garcia, 1969: Cloud height contouring from Apollo-6 photography. *Bull. Amer. Meteor. Soc.*, **50**, 522-528.

気象衛星によるステレオ高度計算法の原理と雷雲上に発生する成層圏内巻雲への応用

藤 田 哲 也

Department of Geophysical Sciences, University of Chicago

静止衛星画像を使って近似的に精度の高いステレオ高度計算法を開発し，日本の“ひまわり”1号とアメリカの静止西衛星の写真から熱帯収束帯附近の雲の高さを計算した。またアメリカの西と東の静止衛星画像を使って雷雲頂の凹凸を赤外温度分布と比較決定した。その結果，赤外温度の方が推定した雲頂温度より5から10°C高いことが分った。

その原因は，かなとこ雲の上空1から3kmの高さの成層圏下部に存在する巻雲が赤外放射温度を見かけ上高めるためで，巻雲の様相は1971年から1978年にかけて行われたLear Jet実験観測によって何度も確認，撮影されている。その巻雲は，ドーム型に突出した雲頂がかなとこ雲の中に急激に下降する時，ドームの風下側に発生する。比較的温度の高い巻雲におおわれた突出ドームの赤外温度は，ドームそのものの温度より可成り高いので，赤外温度の上昇がドームの沈下のためかそれとも巻雲の増加によるものかを放射温度測定だけで判定する事は困難である。